Progress In Electromagnetics Research C, Vol. 167, 104–116, 2026 PIER C

(Received 16 January 2026, Accepted 4 February 2026, Scheduled 16 March 2026)

Multiband Characteristic of a Microwave Triangular Patch Antenna with Harmonic Suppression Capability

Ammar D. Abd Azis[1], Shipun A. Hamzah[1,*], Khairun N. Ramli[1], Bilal A. Khawaja[2],
Saeed Alzahrani[3], Mohd Noh Dalimin[4], and Muhammad S. Yahya[5]

[1]*Faculty of Electrical and Electronic Engineering, Universiti Tun Hussein Onn Malaysia, Parit Raja, Malaysia*
[2]*Faculty of Engineering, Islamic University of Madinah, Kingdom of Saudi Arabia*
[3]*Faculty of Engineering, University of Tabuk, Kingdom of Saudi Arabia*
[4]*Institute of Strategic Science and Technology, Universiti Muhammadiyah Malaysia, Perlis, Malaysia*
[5]*Faculty of Engineering, Universiti Teknologi PETRONAS, Seri Iskandar, Perak, Malaysia*

ABSTRACT: In this paper, a multi-band patch antenna with harmonic suppression capability is developed for LoRa and GPS applications. The antenna configuration consists of a triangular patch as the primary radiator and a microstrip feed line as the excitation source. A parasitic element and a U-shaped slot are incorporated to generate the second and third resonance bands, while two stubs suppress the unwanted harmonics and improve impedance matching. The antenna is implemented on an FR-4 substrate ($\varepsilon_r = 4.4$), consisting of a main radiator, measuring 84.5 mm × 92.45 mm, a parasitic element of 56 mm × 6.2 mm, a U-slot of 35 mm × 1.8 mm, and two stubs, measuring 7 mm × 3 mm and 15 mm × 3 mm. The antenna's width and length are both 140 mm with a 50-Ω feed line of width 3 mm and length 19.5 mm. The bottom of the antenna contains a full ground plane. An extensive parametric study is conducted to optimize the antenna. The simulation and measurement results confirm that the antenna meets the -10 dB return-loss criterion throughout its operating frequencies with a bandwidth of 19 MHz (426–445 MHz) for the 433-MHz band, 13 MHz (916–929 MHz) for the 923-MHz band, and 19 MHz (1.559–1.578 GHz) for the 1.57-GHz band. The unwanted harmonics at 1.68 GHz, 2.00 GHz, and 2.67 GHz are successfully attenuated. The simulated current distributions, radiation patterns, and gain values for each band validate the antenna's multiband operation and harmonic-suppression capability.

1. INTRODUCTION

Long Range (LoRa) [1, 2] stands out as one of the most impactful communication technologies in modern Internet of Things (IoT) technology. It allows IoT sensors to transmit data efficiently by enabling long-range low-power communication. It is also widely implemented in smart cities, smart agriculture, asset tracking, and environmental monitoring, making it essential for automation, intelligent services, and operational efficiency [1, 2]. The combination of LoRa with LoRa Wide Area Network (LoRaWAN) protocol enables stable, energy-efficient, and low-cost data transmission without relying on conventional cellular networks [2, 3]. The growing use of IoT in industrial monitoring and smart cities has increased the demand for long-range, low-power networks. Operating on unlicensed frequency bands of 433 MHz, 868 MHz, and 915 MHz, LoRa supports low data rates with minimal power usage, making it ideal for wide IoT networks.

LoRaWAN has become the platform of choice for sensor networks, M2M systems, environmental monitoring, and smart city services because it has a communication range of up to 15 km in rural areas and the capacity to support thousands of devices concurrently [3, 4]. The combination of LoRaWAN and GPS has a significantly positive impact on logistics, agriculture, and security applications [4].

The demand for compact, efficient antennas that operate across multiple bands in LoRa systems is increasing with the continuous development of smart cities and industrial automation. However, the existing LoRa antennas are monoband with limited harmonic suppression capability. Ref. [5] shows a lack of compact multiband designs capable of supporting 433 MHz, 868/915 MHz, and GPS 1.57 GHz. To address this gap, this work presents a compact triangular patch triple-band antenna operating at 433 MHz (LoRa), 923 MHz (LoRa), and 1.57 GHz (GPS). The proposed antenna design in this work utilizes parasitic elements, etched slots, and tuning stubs to efficiently create resonant modes and attenuate unwanted harmonic frequencies.

The past literature study on LoRa networks, LoRa antenna designs, and GPS systems can be found in [5–7]. A microstrip patch antenna is a compact, planar radiator consisting of a metallic patch printed on a dielectric substrate backed by a ground plane. Radiation occurs primarily due to fringing fields at the patch edges, while the resonant frequency and input impedance at the feed point are governed by the patch geometry, substrate characteristics, and feed location. The input impedance at the patch edge is usually in the range of 200–300 Ω and can be transformed to approximately 50 Ω through the use of an inset-feed technique. Patch antennas are very suitable for compact wireless devices due to their lightweight struc-

---

[*] Corresponding author: Shipun Anuar Hamzah (shipun@uthm.edu.my).

doi:10.2528/PIERC26011603

Published by THE ELECTROMAGNETIC ACADEMY

ture, low manufacturing cost, and easy integration with planar circuits. Recently, researchers have been focusing on broadband development and performance enhancement, as well as multiband and reconfigurable functions, achieved through several techniques such as slot integration, defected ground structures, metamaterial loading, and machine learning-driven optimization.

Triangular patch antennas [8, 9] have the potential to support multiple resonance modes due to their different geometric shapes, making them attractive for multi-band operation and size reduction. These antennas provide a good combination of compactness, high performance, and multiband capability for mobile wireless applications when refined with slot [8] or defective ground plane [9] methods. In a conventional patch, the second resonance is difficult to control because it is sensitive to changes in the antenna structure. Parasitic element [8–10] is used to allow a specific current to pass without altering the main structure of the antenna. It is basically used at the edges of the patch to create capacitive coupling with the main radiator. The effective electrical length of the patch is altered, causing additional resonant frequencies to occur. The second and third operating bands can be stabilized more effectively by modifying the length, placement, and spacing of parasitic elements. This method can help increase the number of bands while maintaining a small antenna size.

The researchers in [11] used inverted L-shaped and T-shaped parasitic elements to create a compact antenna with a stable radiation pattern for LTE, WLAN, and WiMAX applications. A similar concept has been applied by the researchers in [12] to dual-band antennas for 868 MHz and GPS, where a single parasitic element introduces the second resonance while maintaining small antenna size with stable excitation. An elliptical characteristic mode analysis (CMA)-based antenna was introduced by [13], which integrates four triangle-shaped arms to support 2G to 5G sub-6 GHz bands. The use of slots [14–16] in antenna design also helps to produce multiple bands. Slots are capable of altering the current path to generate additional required bands. There are several slot shapes that can be used, such as linear, U-shaped, or split-ring ones for the purpose of longer or disconnected current paths. This method indirectly changes the resonant frequency by increasing the electrical length of the antenna. Therefore, 433 MHz, 923 MHz, and 1.57 GHz can be generated using slots without enlarging the patch, while maintaining a stable radiation pattern and good impedance matching. Researchers in [17, 18] have studied substrate integrated waveguide (SIW)-based slots and split-ring slots to obtain up to five bands. However, high fabrication accuracy is required to design these slots. Unlike [19], slot-loaded patch antennas can achieve a maximum of six bands with high gain, although their performance is highly affected by fabrication tolerances for millimetre wave applications. The right-angle slot and tuning stub designed by [20] found an almost omnidirectional pattern while obtaining a maximum of four bands. However, [21, 22] combine low/high modes with an L-shaped slot to produce multi-bands that are stable across low to mid frequencies. However, designs that use slots have problems controlling unwanted frequency changes, which require precise structural control. A dual-band slot antenna with a feed line slot is an example of an antenna design that can improve efficiency, although the FR-4 substrate still has limitations due to large physical size [23].

A multi-band antenna operating at closely spaced resonant frequencies requires more detailed harmonic suppression to ensure that only the desired frequencies can be used effectively. Several techniques can be used to suppress harmonics, such as external filters, feed network modifications, and reactive structures, like tuning stubs. Tuning stub [24] is used to disrupt surface currents at targeted locations to prevent the formation of higher-order resonances while maintaining the fundamental mode. It creates an impedance discontinuity in that area, thereby enabling destructive interference at harmonic frequencies. Stubs placed near the edge of the patch or along the feed line can modify the current path and reactive loading to control selected harmonics without increasing the complexity of the patch. This method can effectively suppress harmonics and provide the required band isolation. The authors in [25] proposed a patch antenna with different feeds that can suppress harmonics up to 3.4 times the frequency while maintaining the required gain and bandwidth.

In dipole systems, parasitic elements and tuning stubs effectively suppress harmonics in the 3–5 GHz range while preserving dual-band operation at 0.8 GHz and 2.4 GHz, though physical size increased [26]. However, this feeding method results in a more complex antenna structure. Current path modification as an effective technique without compromising radiation performance has been carried out using dipoles for single-band [27], dual-band [28], and triple-band [29], capable of achieving harmonic suppression using an integrated stub. A wide range of multi-band antenna designs has been presented in the literature, encompassing monopole and metamaterial-inspired monopoles [29, 30], patch and multi-layer patch structures [31, 32], multiple-input multiple-output (MIMO) arrangements [33], bow-tie configurations [34], and machine-learning-assisted methods [35]. Overall, previous researchers have used various approaches to improve efficiency, expand bandwidth, and optimize antenna performance.

In this work, the proposed antenna's operating frequencies, bandwidth, radiation pattern, and gain are simulated using Computer Simulation Technology (CST) Microwave Studio simulation software. Parametric studies and current-distribution analysis have been done to provide insight into its operating mechanisms before fabrication and measurement are conducted to validate real-world performance.

2. PROPOSED DESIGN

The proposed antenna is designed to support multi-band wireless communication with harmonic suppression capability. It was designed using an organized approach combining analytical electromagnetic theory and full-wave parametric study optimization. Initially, the design process was started with a 50 Ω input impedance requirement to ensure compatibility with the standard radio frequency (RF) systems. Figure 1 depicts the proposed antenna, comprising a triangular patch fed by a microstrip line and integrated with parasitic elements, a slot, and two stubs. The main triangular patch was initially sized for

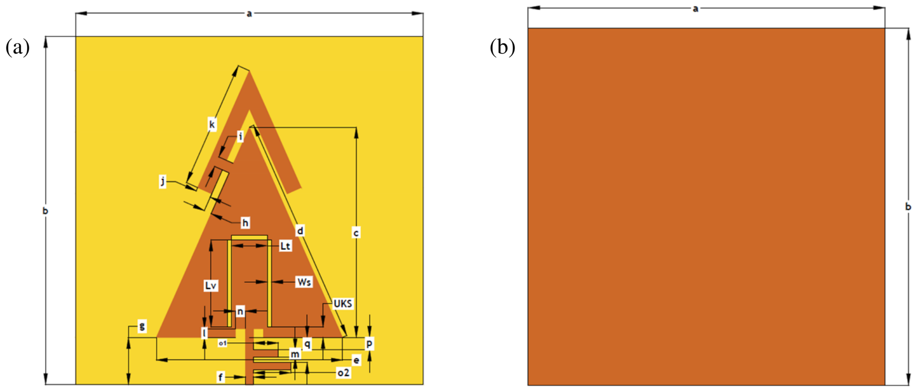

FIGURE 1. Structure of the proposed antenna. (a) Front view. (b) Back view.

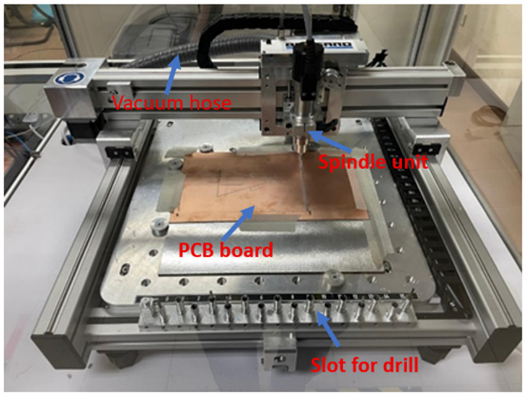

FIGURE 2. Computer-controlled drilling machine.

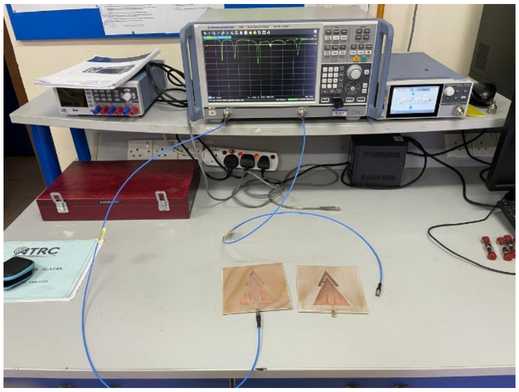

FIGURE 3. Rohde & Schwarz VNA.

923 MHz using microstrip principles, where resonance depends on the effective electrical length and quarter guided wavelength ($\lambda_g/4$) along the patch height (c). In addition, c was optimized iteratively to tune the resonance while maintaining good impedance matching. The triangular geometry is chosen for its compact size, ease of polarization control, and superior broadband performance relative to conventional rectangular patches. Three main conductors, along with two stubs, are placed on the top surface of the substrate, while the bottom layer serves as a full ground plane. For the 433 MHz lower band, a parasitic element was attached to the main patch, extending the current path to achieve $\lambda_g/2$ resonance. The key dimensions of connector height (h), parasitic width (j), and length (k) were optimized to ensure stable resonance without interfering with the 923 MHz band. The 1.57 GHz band was introduced via a U-shaped slot on the triangular patch, creating an additional resonant path. The slot's bridge length (L_T), leg length (L_V), width (W_S), and position (UKS) were optimized based on the guided wavelength principle to precisely tune the resonance while minimizing interference with lower bands. Hereafter, the antenna is referred to as Antenna A. Finally, two open-ended stubs were added along the feed line to suppress unwanted higher-order resonances at 1.68 GHz, 2.0 GHz, and 2.67 GHz. Stub lengths (o_1, o_2) and positions (p, q) were optimized according to quarter guided wavelength transmission-line theory to align the notch frequencies without affecting the desired bands. Hereafter, the antenna is denoted as Antenna B. An FR-4 substrate with a relative permittivity of 4.6 and thickness of 1.6 mm is used.

Antenna A and Antenna B were fabricated using a Bungard CCD2 dry etching machine with a typical resolution of approximately 0.1 mm. The fabrication procedures import the Gerber files from CST to the drilling machine's computer, preparing the printed circuit board (PCB) substrate and drill bits, and executing the milling process from the computer. Compared with conventional chemical etching, this approach avoids the use of hazardous chemicals, requires minimal workspace, and achieves improved fabrication accuracy and consistency.

After the fabrication process, the reflection coefficient (S_{11}) of both antennas was measured using a Rohde & Schwarz vector network analyzer (VNA) operating up to 20 GHz. The VNA was calibrated prior to measurement, and each antenna was connected using a 50-Ω coaxial cable. All measurements were carried out under laboratory conditions at the Advanced Telecommunication Research Center (ATRC), a Centre of Research (CoR) within the Faculty of Electrical and Electronic Engineering (FKEE), Universiti Tun Hussein Onn Malaysia (UTHM). Figure 2 depicts that the computer-controlled drilling machine consists of a vacuum hose, a spindle unit, and a slot for drill. Figure 3 portrays the Rohde & Schwarz VNA used in the measurement.

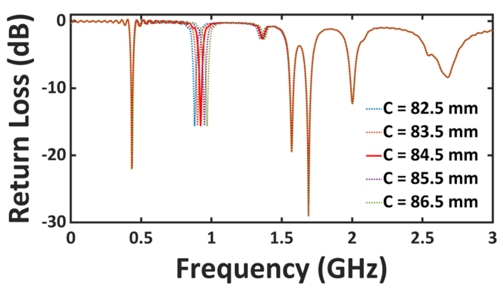

FIGURE 4. Parametric study of triangle height, c.

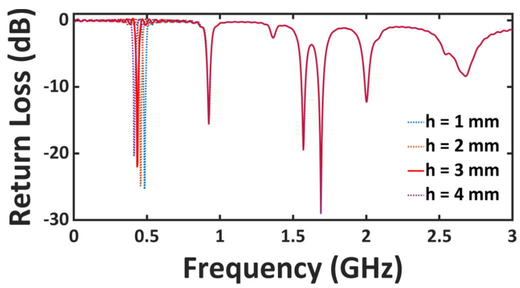

FIGURE 5. Parametric study of connector height, h.

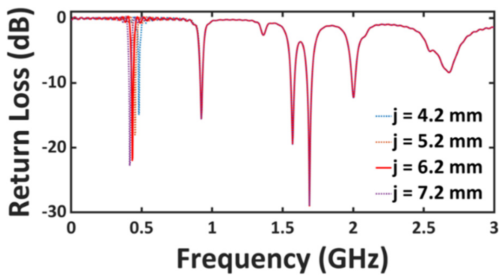

FIGURE 6. Parametric study of parasitic width, j.

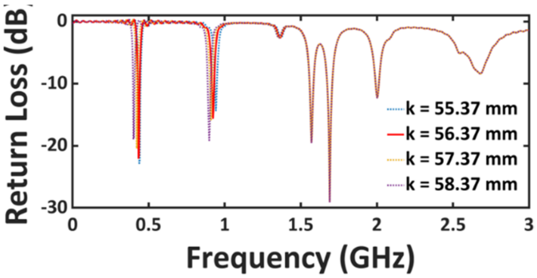

FIGURE 7. Parametric study parasitic length, k.

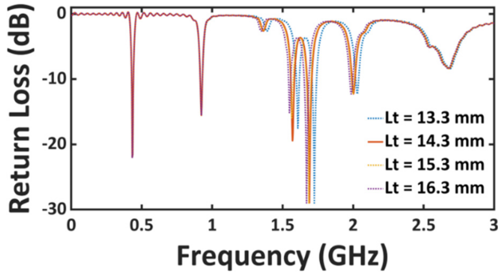

FIGURE 8. Parametric study bridge top length, L_t.

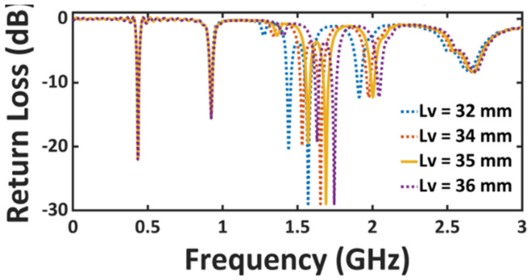

FIGURE 9. Parametric study of bridge top length, L_v.

The antenna is designed to operate at three primary frequency bands: 433 MHz (433.05–434.79 MHz), 923 MHz (920–923 MHz), and 1.57 GHz (GPS; BW $\approx$ 2 MHz). The desired performance targets include a return loss below -10 dB, bandwidth coverage for LoRa and GPS, near-omnidirectional radiation patterns, and a gain above 1 dBi. Overall, the initial dimensions were derived from electromagnetic theory, and the final geometry was achieved through parametric refinement to realize the triple-band antenna performance. A detailed parametric study is conducted to determine the optimal parameters for each band. The analysis reveals that parameter a governs the 433 MHz resonance, and parameters b and c influence the 923 MHz band, while parameters d, e, and f determine the 1.57 GHz resonance. The findings for each band are summarised below.

2.1. LoRa Band 923 MHz

Figure 4 shows that varying parameter c from 82.5 to 86.5 mm significantly affects the 923 MHz resonance. The optimal length is $c = 84.5$ mm, resulting in a return loss of approximately -15.5 dB while maintaining stable resonances at 433 MHz and 1.57 GHz.

2.2. LoRa Band 433 MHz

In Figure 5, the parametric study indicates that the connector height h (1–4 mm) influences the 433 MHz response. The optimal value $h = 3$ mm yields a return loss of -21.98 dB, demonstrating excellent impedance matching.

Figure 6 shows that the width of the parasitic element j affects the 433 MHz resonance through variations in current coupling. The optimal width $j = 6.2$ mm achieves a return loss of -23 dB.

The length of the parasitic element k (55.37–58.37 mm) also tunes the 433 MHz band by altering the effective current path. The optimal length $k = 56.37$ mm achieves a return loss of -22 dB and maintains stable performance across all operating bands. The results obtained are presented in Figure 7.

2.3. GPS Band 1.57 GHz

The upper-bridge length L_t (13.3–16.3 mm) significantly affects the 1.57 GHz resonance, as shown in Figure 8. The optimal value $L_t = 14.3$ mm achieves a return loss of -19.4 dB, while the 433 MHz and 923 MHz bands remain stable.

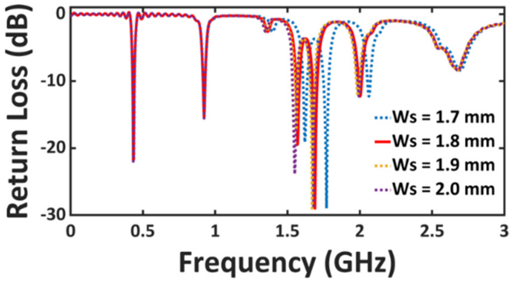

FIGURE 10. Parametric study of the slot width, W_s.

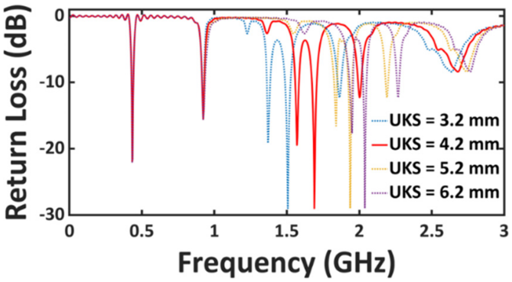

FIGURE 11. Parametric study of the distance between the slot and the base of the triangular patch, *UKS*.

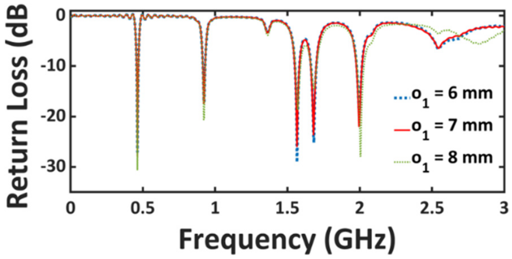

FIGURE 12. Parametric study of stub 1 length, O_1.

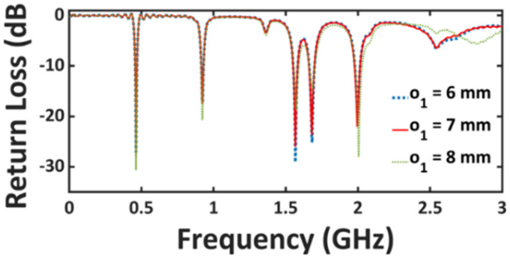

FIGURE 13. Parametric of stub 1 position, p.

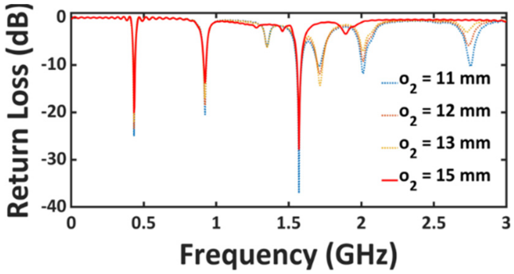

FIGURE 14. Parametric study of stub 2 length, O_2.

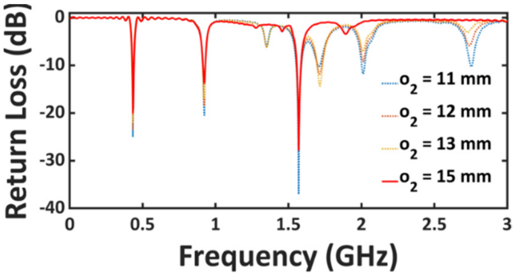

FIGURE 15. Parametric study of stub 2 position, q.

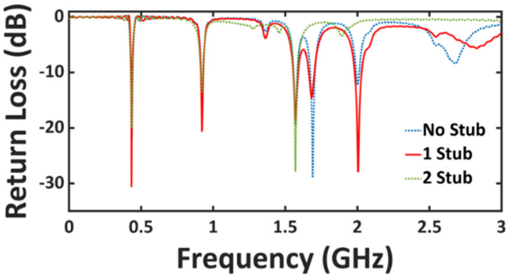

FIGURE 16. Simulated return-loss results for the proposed antenna under three configurations: without a stub (blue), with one stub (red), and with two stubs (green). The antenna operates at 433 MHz, 923 MHz, and 1.57 GHz, while the harmonic frequencies at 1.68 GHz, 2.0 GHz, and 2.67 GHz are effectively suppressed, exhibiting return-loss levels of -2 dB, -1.5 dB, and -1.0 dB, respectively.

In Figure 9, the U-slot leg length L_v (32–36 mm) is observed to influence the GPS resonance. The optimal value $L_v = 35$ mm yields a return loss of -19.4 dB.

The U-slot width W_s also contributes to tuning by modifying the slot capacitance. The optimal width $W_s = 1.8$ mm achieves a return loss of approximately -19.4 dB. The results obtained are presented in Figure 10.

Another important parameter is the U-slot offset from the base (*UKS*), tested between 3.2 and 6.2 mm. The optimal distance $UKS = 4.2$ mm provides the best impedance match for the 1.57 GHz band. The results obtained are presented in Figure 11.

2.4. Harmonic Suppression at 1.68 GHz, 2.0 GHz and 2.67 GHz

Figures 12 and 13 show the effect of stub-1 length (O_1) and position (p) on suppressing the 2.67 GHz harmonic. The optimal values $O_1 = 7$ mm and $p = 5$ mm deliver the most effective suppression without disrupting the primary resonances.

Figures 14 and 15 analyse stub-2, where the length (O_2) and position (q) significantly influence harmonic suppression at 1.68 GHz and 2.0 GHz. Optimal suppression is achieved with $O_2 = 15$ mm and $q = 15$ mm, while preserving overall frequency selectivity.

Figure 16 presents the simulated return-loss response of the antenna. Harmonic suppression is obtained by tuning the stub length to roughly a quarter wavelength, while the stub width, terminal length, and placement are further optimized as outlined earlier.

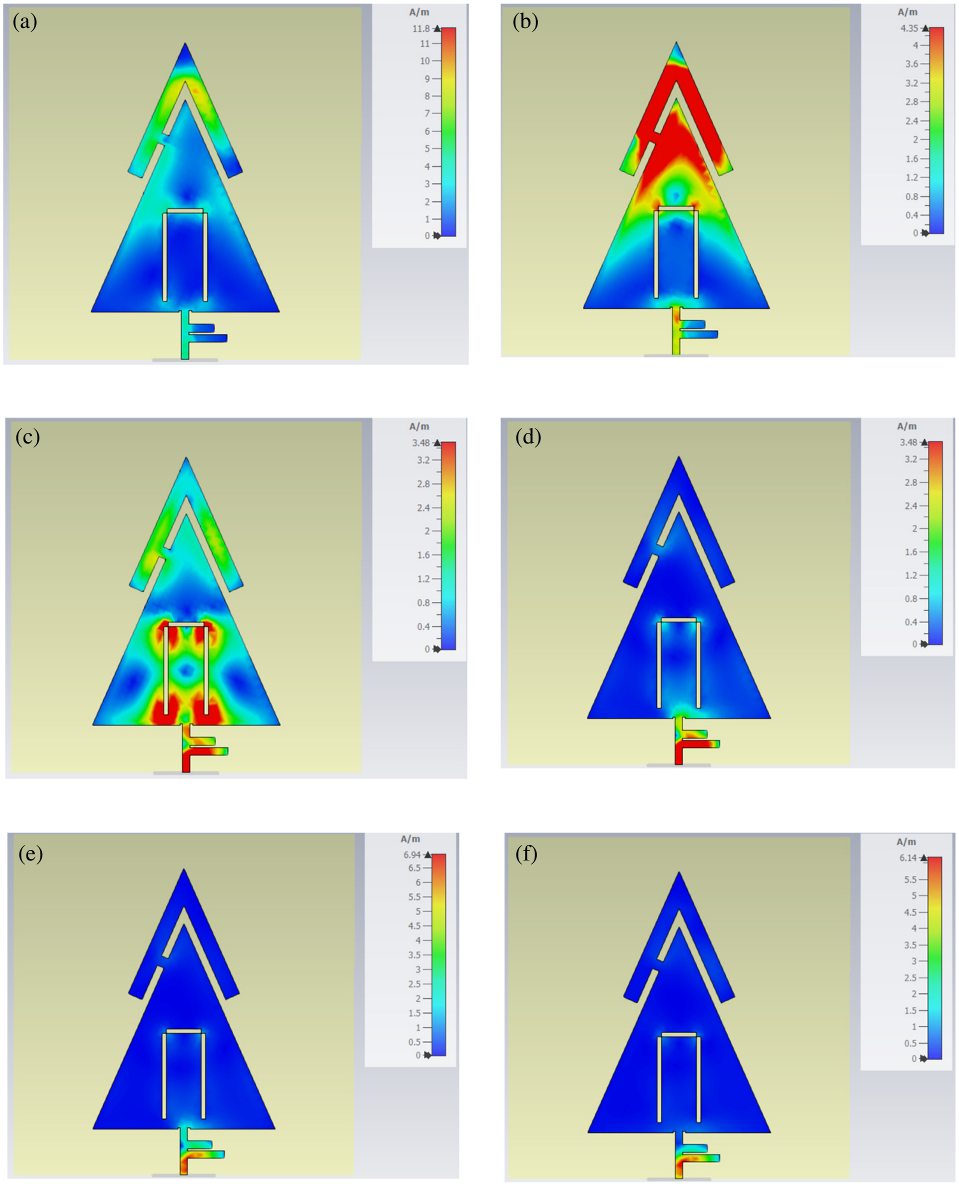

FIGURE 17. Current distribution of antenna, (a) at 0.923 GHz, (b) at 0.433 GHz, (c) at 1.57 GHz, (d) at 1.68 GHz, (e) at 2.00 GHz, (f) at 2.67 GHz.

2.5. Current Distribution Analysis

To assess the effectiveness of the harmonic suppression mechanism, current distribution analyses are conducted, as shown in Figure 17. In Figure 17(a), a strong current concentration on the parasitic element confirms excitation at 433 MHz. Figure 17(b) shows dominant current flow on the main radiator at 923 MHz, while Figure 17(c) reveals current concentration around the U-slot, validating operation at 1.57 GHz. These results are consistent with the observed return loss measurements.

Figures 17(d)–(f) show strong current concentration on both stubs, indicating that the current is diverted away from the radiating element at 1.68 GHz, 2.0 GHz, and 2.68 GHz. As a result, no radiation occurs at these frequencies, confirming effective harmonic suppression consistent with the return-loss characteristics in Figure 4. The findings from the parametric analysis enable the precise determination of the optimal antenna parameters, summarised in Table 1.

The antenna prototype is fabricated using a dry-etching technique to ensure dimensional precision and conductor quality. It is then measured to assess actual performance, including return loss, radiation patterns, and gain. These measurements confirm the simulation results and demonstrate that the antenna meets the expected performance based on the optimized design parameters.

2.6. Equivalent Circuit Modeling and Validation

The physical behavior of the multi-band antenna is characterized using a Lumped Element Equivalent Circuit (LEEC) model to provide a deterministic link between physical parameters and electromagnetic resonances at 433 MHz, 923 MHz, and 1.57 GHz. This section discusses the RLC formation modeled in Advanced Design System (ADS), the impact of physical geometry, and the validation of the model against simulation and measured data.

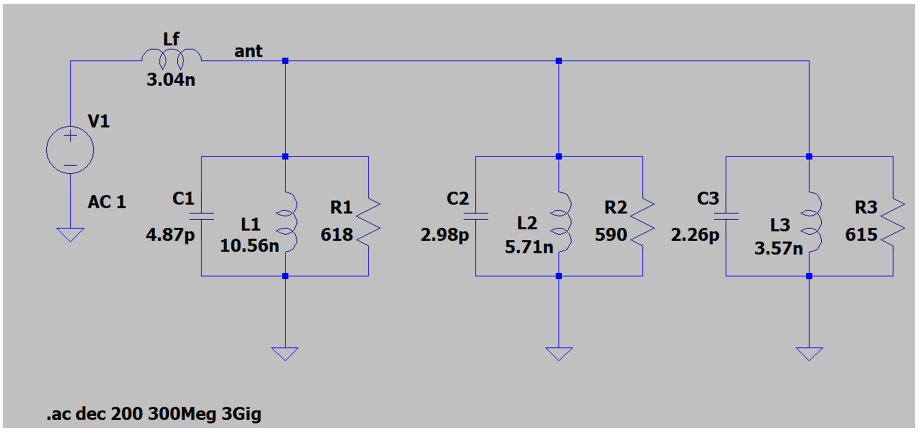

FIGURE 18. Equivalent circuit of Antenna A.

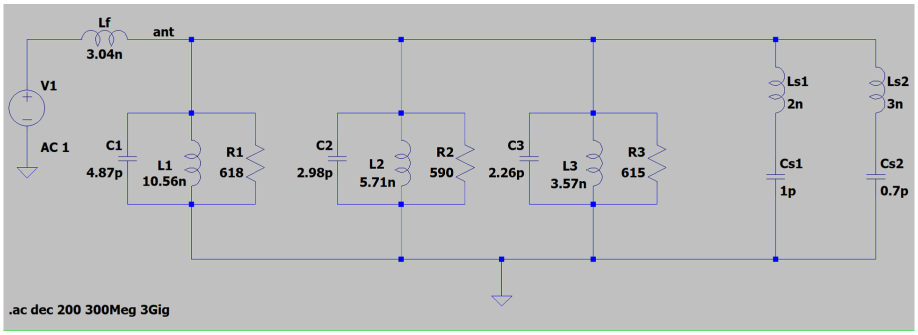

FIGURE 19. Equivalent circuit of Antenna B.

TABLE 1. Parameters of the designed antenna.

Element	Symbol	Value (mm)
Substrate Size	$a \times b$	140×140
Triangle Height	c	82.5
Triangle Side	d	92.45
Triangle Width	e	76
Feed Width	f	3
Feed Length	g	19.5
Connector Height	h	5
Connector Width	i	4.2
Parasitic Width	j	6.2
Parasitic Length	k	58.34
Notch Depth	l	0.5
Notch Width	n	1
Stub Width	m	3
Stub 1 Length	o_1	7
Stub 2 Length	o_2	15
Stub 1 Position	p	5
Stub 2 position	q	9
Bridge Top Length	L_t	14.3
U-Slots Legs	L_v	35
Slot Width	W_S	1.8
Distance Slot from Base	UKS	4.2

2.6.1. Physical-to-Electrical Mapping and RLC Formation

As illustrated in the equivalent circuit of Antenna A depicted in Figure 18, the antenna's structural discontinuities are represented as a network of reactive components, where each resonant band is modeled as a parallel RLC tank circuit (R_n, L_n, C_n) derived from the energy storage and dissipation characteristics of the patch.

The Low-Frequency Resonance (433 MHz) is primarily governed by the interaction between the main patch and parasitic elements j and k, where variations in the parasitic width and length alter the surface current distribution, modeled by the primary inductance L and capacitance C. In contrast, the Intermediate Resonance (923 MHz) is stabilized by the patch length c and secondary geometry L_t; these dimensions define the radiation resistance R_2, ensuring proper impedance matching for the LoRa/Biomedical IoT band. Finally, the High-Frequency Resonance (1.57 GHz GPS) is heavily dependent on the U-slot configuration, specifically the leg length L_v, width W_s, and offset UKS. Within this band, the slot width modifies the gap capacitance C_3 while the offset UKS determines the input impedance matching R_3 for optimal GPS performance as presented in the third RLC branch of Figure 18.

2.6.2. Harmonic Suppression and Mathematical Modeling

The equivalent circuit for Antenna B, as shown in Figure 19, incorporates series-resonant branches (Ls_1Cs_1 and $Ls_{12}Cs_2$) to suppress unwanted harmonics at 1.68 GHz, 2.0 GHz, and 2.67 GHz. Within the ADS environment, these branches act as band-stop filters by creating a low-impedance path to the ground plane at harmonic frequencies. The total input

TABLE 2. The summary of physical feature, dominant RLC parameter, and the targeted band of the antenna.

Physical Feature	Dominant RLC Parameter	Target Band/Function
Parasitic Elements (j, k)	Inductance (L_1), Capacitance (C_1)	433 MHz Resonance
Patch Length (c, L_t)	Radiation Resistance (R_2)	923 MHz Stability
U-slot Geometry (L_v, W_s, UKS)	Slot Capacitance (C_3), Resistance (R_3)	1.57 GHz Tuning
Feed Height (h)	Series Inductance (L_f)	Fundamental Matching
Tuning Stubs (Antenna B)	Series LC Resonators (L_s, C_s)	Harmonic Suppression

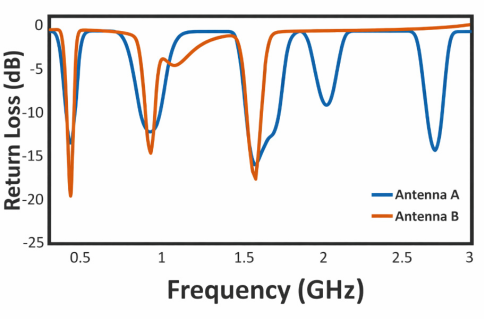

FIGURE 20. Return loss result of the equivalent circuit of Antenna A and Antenna B.

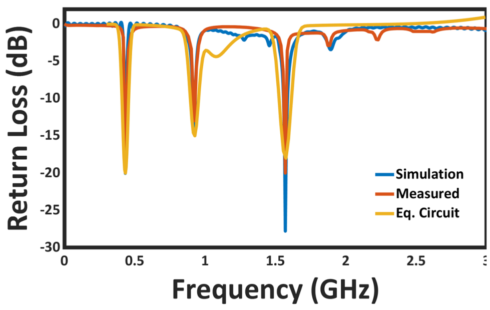

FIGURE 21. Simulated, measured, and equivalent circuit S_{11} results of Antenna B.

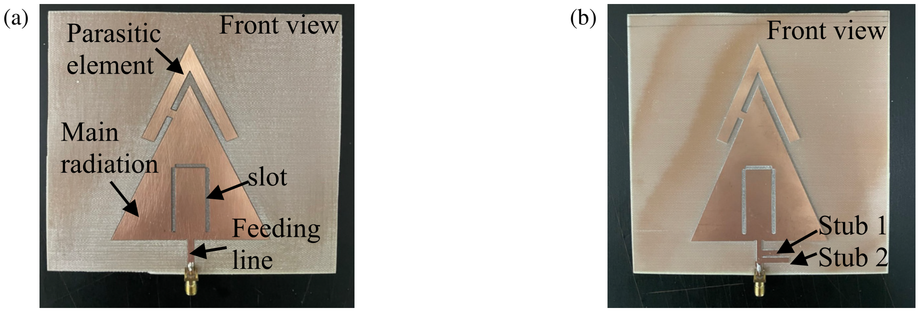

FIGURE 22. Fabricate antenna. (a) Antenna A. (b) Antenna B.

impedance Z_{in} is calculated by considering the series feed inductance l_f and the parallel admittance of the resonant tanks:

$$Z_{in} = j\omega L_f + \left[\sum_{i=1}^{3}\left(\frac{1}{R_i} + j\omega C_i + \frac{1}{j\omega L_i}\right) + Y_{stub}\right]^{-1} \tag{1}$$

2.6.3. Comparison of S_{11} Curves and Validation

The validation of LEEC models for Antenna A and Antenna B was performed by comparing reflection coefficient (S_{11}) results with full-wave CST simulations and experimental measurements. As shown in Figure 20, both models accurately capture the primary frequencies at 433 MHz, 923 MHz, and 1.57 GHz. However, Antenna B circuit effectively suppresses resonances near 2.0 GHz and 2.67 GHz that are present in Antenna A, validating the role of the series-resonant stubs added. Figure 21 demonstrates a strong correlation among the ADS LEEC model, CST simulation, and measured data for Antenna B, with all three targeted bands remaining significantly below the -10 dB threshold. Minor deviations in return loss magnitude are attributed to simplified lumped elements not accounting for all parasitic coupling present in the physical environment.

2.6.4. Summary of Design Relationships

The correlation between physical design variables and their respective roles in the LEEC model is summarized in Table 2.

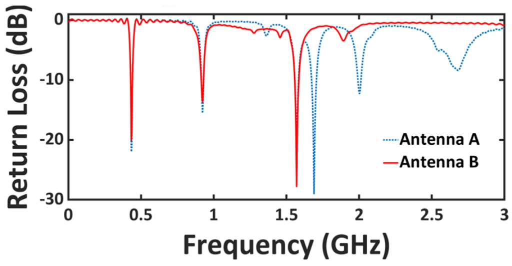

FIGURE 23. Measured result of Antenna A and Antenna B.

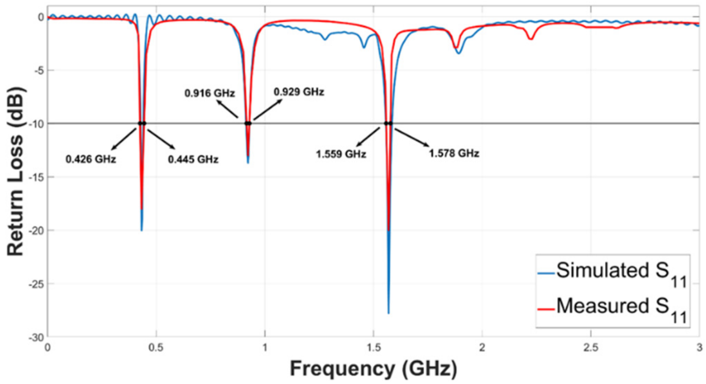

FIGURE 24. Comparison between simulated and measured S_{11} of Antenna B.

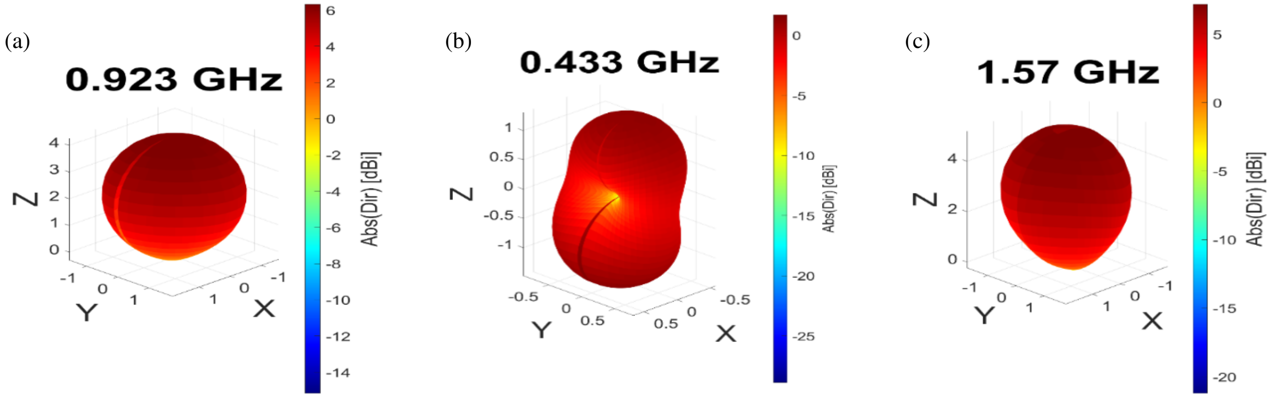

FIGURE 25. 3D radiation pattern of Antenna B, (a) at 0.923 GHz, (b) at 0.433 GHz, (c) at 1.57 GHz.

3. RESULTS AND DISCUSSION

Figures 22(a) and 22(b) show antennas fabricated via dry etching: (a) without stubs (Antenna A) and (b) with two stubs (Antenna B). Both images show the top view, with the bottom as a full ground plane.

Figure 23 compares the measured return loss of the two prototypes. The antenna without stubs in Figure 22(a) operates at six resonance frequencies, 433 MHz, 923 MHz, and 1.57 GHz, along with three unwanted harmonic modes at 1.68 GHz, 2.0 GHz, and 2.28 GHz. After integrating the two stubs, as shown in Figure 22(b), these harmonic frequencies are completely suppressed, as evidenced in Figure 23. The results verify that the final antenna design achieves the intended triple-band operation at 433 MHz, 923 MHz, and 1.57 GHz, while also offering excellent harmonic suppression. The final results of the return loss as presented in Figure 24 shows that the simulation and measurement have a good agreement.

Figure 24 shows the simulated and measured return losses of Antenna B, with good agreement between them.

Figures 25(a)–(c) present the simulated 3D radiation patterns of the optimized antenna for the three operating bands. The results demonstrate that the antenna maintains a near-omnidirectional radiation characteristic across all frequencies, fulfilling the requirements of LoRa and GPS applications that demand consistent and wide-area coverage.

Due to the limitations of the anechoic chamber, which can measure frequencies above 500 MHz, only the 3D pattern results for the 923 MHz and 1.57 GHz frequency bands are presented in this article. Figure 26 shows the 3D radiation patterns of Antenna A and Antenna B at 923 MHz and 1.57 GHz in bottom, front, and top views. At 923 MHz, both antennas exhibit quasi-omnidirectional patterns with moderate main lobes and stable azimuthal distribution. Antenna A records magnitudes of -26.66 dB and -20.89 dB, with phase values of 81.94° and -166.45°, for H-plane and E-plane, respectively. Antenna B shows comparable results with -26.75 dB and -20.95 dB, with phase values of 84.84° and -158.93°, for H-plane and E-plane, respectively. The close agreement indicates consistent radiation pattern and polarization behavior. At 1.57 GHz, both antennas become more directional with a more concentrated main lobe. Antenna A achieves -19.47 dB and -16.82 dB, with phase values of -178.87° and -152.69°, for H-plane and E-plane, respectively. Antenna B shows -28.44 dB and -16.64 dB, with phase values of -81.4° and -120.97°, for H-plane and E-plane, respectively. The increased directivity at this frequency is attributed to the excitation of higher-order or slot-induced resonant modes. Overall, both antennas demonstrate stable quasi-omnidirectional radiation at 923 MHz and enhanced directivity at 1.57 GHz, confirming consistent multi-band performance.

The simulated gain values at the three bands of Antenna B and Antenna A are (433 MHz $=$ 5.29 dBi), (923 MHz $=$ 8.52 dBi), and (1.57 GHz $=$ 5.88 dBi), respectively, as depicted in Figure 27. These values indicate adequate radiation

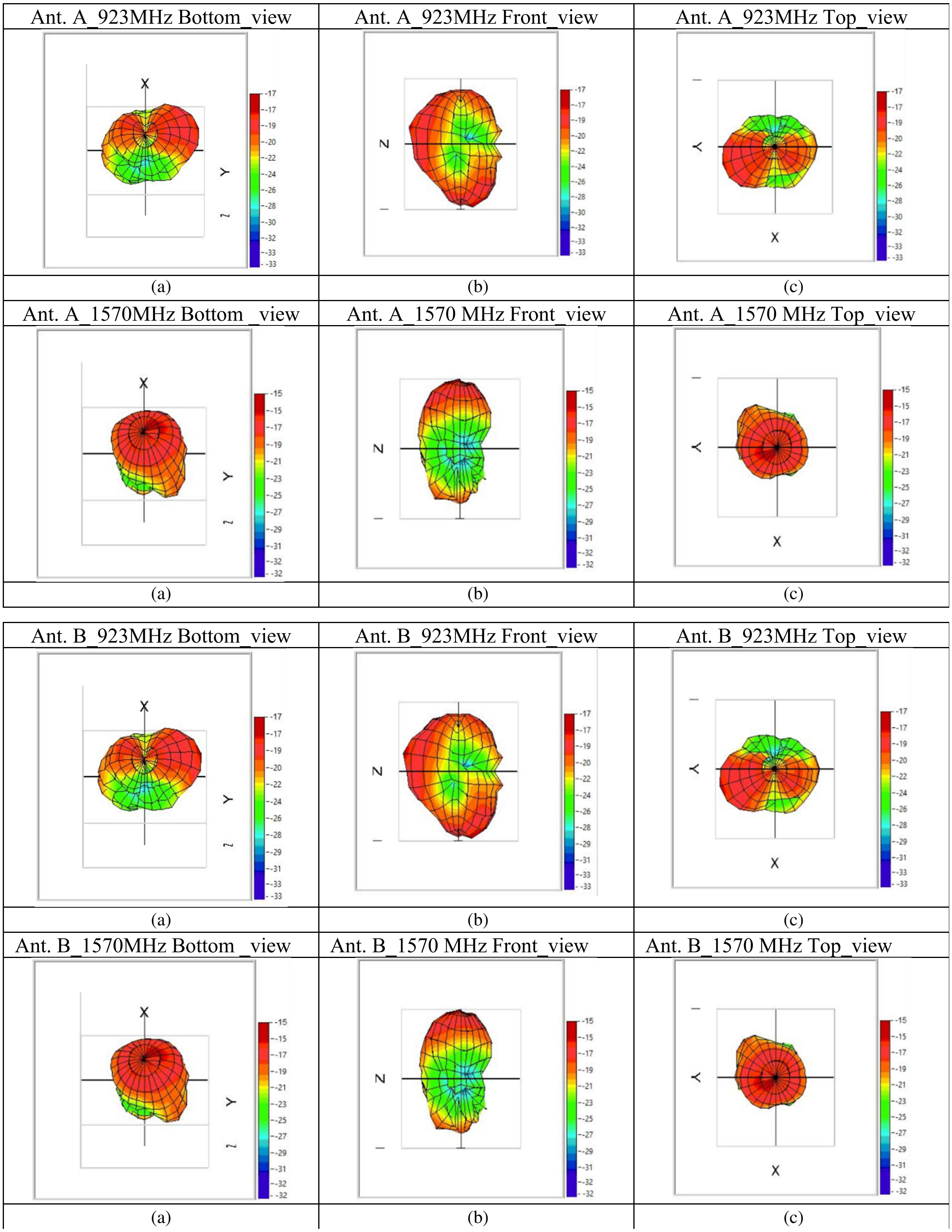

FIGURE 26. Measured 3D radiation patterns of Antenna A and Antenna B at 923 MHz and 1.57 GHz. (a) Bottom view. (b) Front view. (c) Top view.

performance suitable for low-power, long-range wireless systems. The stable radiation pattern and gain across all bands verify that the proposed antenna design is well-suited for integrated LoRa-GPS functionality in modern IoT environments. In the 1.6–3 GHz range, the gain drops significantly due to harmonic suppression, causing Antenna B to radiate ineffectively at these frequencies.

The proposed antenna, in comparison with other designs reported in the literature, is presented in Table 3. The proposed antenna addresses harmonic suppression, stable multi-

TABLE 3. Comparison of the proposed antenna with designs published in the literature.

Ref.	Year	No of band	Ant. Type	Method	Freq. (MHz)	Board	Harmonic Freq. Suppression	Gain (dBi)
[12]	2013	3	patch	Parasitic elements	2020 2450 3500	FR-4	No	3.6 3.0 8.8
[15]	2013	3	patch	slot and a bridging element	2460 3280 5380	FR-4	No	3.1 4.2 5.6
[9]	2022	3	monopole	metamaterial	3000–4170, 5330–6500, 8900–12000	FR-4	Yes	3.2 4.1 5.0
[10]	2023	2	patch	Fractal geometry	4170 5970	FR-4	No	8.9 9.6
[20]	2023	4	patch	Mode-based	1720 2120 2370 3540	Rogers	No	5.9 7.0 4.5 5.7
[13]	2024	2	patch	Parasitic elements	868 1570	FR-4	No	1.9 3.4
[6]	2024	4	patch	Additional patch	433 868 915	FR-4	No	1.6 2.4 2.6
This work		3	patch	Parasitic element and slot	433 923 1570	FR4	Yes	5.29 8.52 5.88

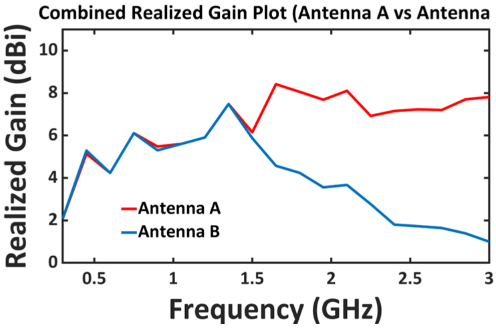

FIGURE 27. Simulated realized gain.

band performance, and higher gain at lower bands, which are the main drawbacks of most existing designs. The combination of parasitic elements and a slot provides enhanced control of resonance and efficiency across the three antenna bands.

4. CONCLUSION AND FUTURE WORK

This study presents the design, simulation, fabrication, and measurement of a compact triple-band antenna featuring efficient harmonic suppression. The antenna is built around a triangular patch resonating at 923 MHz, fed through a $50\,\Omega$ microstrip line. To achieve operation across three distinct frequency bands, the design incorporates a parasitic element and a U-shaped slot. Additionally, two stubs positioned alongside the feed line serve as low-pass filters, effectively mitigating unwanted harmonic signals.

The parasitic element generates the resonant mode at 433 MHz, whereas the U-slot introduces the third operating band at 1.57 GHz, making the antenna suitable for LoRa and GPS applications. The two designed stubs effectively suppress three major harmonics at 1.68 GHz, 2.0 GHz, and 2.68 GHz. The antenna design was guided by CST parametric studies, allowing precise adjustment of each geometrical parameter to achieve the target resonant frequencies. Simulation outcomes were verified by examining current distribution and return-loss characteristics, which showed that currents were concentrated on the radiating elements and stubs as intended. These optimized parameters were subsequently applied during the fabrication process.

Measured results show that the antenna operates stably at all three target frequency bands, 433 MHz, 923 MHz, and 1.57 GHz while the undesired harmonic frequencies at 1.68 GHz, 2.0 GHz, and 2.68 GHz are completely eliminated. The measured return-loss values at these bands are -18 dB, -14 dB, -20 dB, -2.2 dB, -1.5 dB, and -1.0 dB, respectively. The simulated gains of 5.29 dBi, 8.52 dBi, and 5.88 dBi, together with their nearly omnidirectional radiation patterns, further confirm that the proposed antenna performs effectively across all three operating bands. In summary, the results indicate that the developed antenna is highly suitable for integration with LoRa and GPS systems, offering dependable multi-band performance along with efficient harmonic suppression.

ACKNOWLEDGEMENT

This research was supported by Universiti Tun Hussein Onn Malaysia (UTHM) through Tier 1 (vot Q885) and GPPS J041.

REFERENCES

[1] Shafique, K., B. A. Khawaja, F. Sabir, S. Qazi, and M. Mustaqim, "Internet of things (IoT) for next-generation smart systems: A review of current challenges, future trends and prospects for emerging 5G-IoT scenarios," *IEEE Access*, Vol. 8, 23 022–23 040, 2020.

[2] De, S., O. L. Dede, S. Adhinarayanan, H. M. Jalajamony, A. Ibrahim, I. Osunmakinde, and R. E. Fernandez, "Interleaved reception in lora using IFT: A hardware-efficient architecture for fast and low-power image transmission," *IEEE Internet of Things Journal*, Vol. 12, No. 19, 39 777–39 787, Oct. 2025.

[3] Lavdas, S., N. Bakas, K. Vavousis, W. E. Hajj, Z. Zinonos, *et al.*, "Evaluating lorawan network performance in smart city environments using machine learning," *IEEE Internet of Things Journal*, Vol. 12, No. 14, 27 060–27 074, Jul. 2025.

[4] Moshayedi, A. J., A. S. Roy, Z. H. Khan, and S. Yang, "UrbanPark: Advancing parking infrastructure with LoRaWAN-enabled smart parking modules," in *2025 4th International Conference on Computing and Information Technology (ICCIT)*, 7–13, Tabuk, Saudi Arabia, 2025.

[5] Yahya, M. S., S. Soeung, S. K. A. Rahim, U. Musa, S. S. B. Hashwan, Z. Yunusa, and S. A. Hamzah, "LoRa microstrip patch antenna: A comprehensive review," *Alexandria Engineering Journal*, Vol. 103, 197–221, 2024.

[6] Yahya, M. S., S. Soeung, F. E. Chinda, S. K. B. A. Rahim, U. Musa, N. B. M. Nor, and C. Sovuthy, "A compact reconfigurable multi-frequency patch antenna for LoRa IoT applications," *Progress In Electromagnetics Research M*, Vol. 116, 77–89, 2023.

[7] Omali, T. and S. Akpata, "Global positioning system technology: Theory and the methods of its application," *International Journal of Scientific Research in Multidisciplinary Studies*, Vol. 10, No. 5, 70–76, 2024.

[8] Karimbu Vallappil, A., B. A. Khawaja, M. K. A. Rahim, M. N. Iqbal, and H. T. Chattha, "Metamaterial-inspired electrically compact triangular antennas loaded with CSRR and 3×3 cross-slots for 5G indoor distributed antenna systems," *Micromachines*, Vol. 13, No. 2, 198, 2022.

[9] Vallappil, A. K., B. A. Khawaja, M. K. A. Rahim, M. N. Iqbal, H. T. Chattha, and M. F. M. Ali, "A compact triple-band UWB inverted triangular antenna with dual-notch band characteristics using SSRR metamaterial structure for use in next-generation wireless systems," *Fractal and Fractional*, Vol. 6, No. 8, 422, 2022.

[10] Vallappil, A. K., B. A. Khawaja, M. K. A. Rahim, M. Uzair, M. Jamil, and Q. Awais, "Minkowski-Sierpinski fractal structure-inspired 2×2 antenna array for use in next-generation wireless systems," *Fractal and Fractional*, Vol. 7, No. 2, 158, 2023.

[11] Faradi, T., A. Diallo, P. L. Thuc, P. Daragon, and R. Staraj, "Design methods for efficient multiband antennas with parasitic elements," in *2015 9th European Conference on Antennas and Propagation (EuCAP)*, 1–4, Lisbon, Portugal, 2015.

[12] Kim, J.-W., T.-H. Jung, H.-K. Ryu, J.-M. Woo, C.-S. Eun, and D.-K. Lee, "Compact multiband microstrip antenna using inverted-L-and T-shaped parasitic elements," *IEEE Antennas and Wireless Propagation Letters*, Vol. 12, 1299–1302, 2013.

[13] Yahya, M. S., S. Soeung, F. E. Chinda, U. Musa, and Z. Yunusa, "Dual-band GPS/LoRa antenna for internet of thing applications," *Bulletin of Electrical Engineering and Informatics*, Vol. 13, No. 2, 986–995, 2024.

[14] Karimbu Vallappil, A., M. K. A. Rahim, B. A. Khawaja, M. N. Iqbal, N. A. Murad, M. M. Gajibo, L. O. Nur, and B. S. Nugroho, "Complementary split-ring resonator and strip-gap based metamaterial fractal antenna with miniature size and enhanced bandwidth for 5G applications," *Journal of Electromagnetic Waves and Applications*, Vol. 36, No. 6, 787–803, 2022.

[15] Arif, S., S. A. Nasir, M. Mustaqim, and B. A. Khawaja, "Dual U-slot triple band microstrip patch antenna for next generation wireless networks," in *2013 IEEE 9th International Conference on Emerging Technologies (ICET)*, 1–6, Islamabad, Pakistan, 2013.

[16] Sheriff, N., S. Kamal, H. T. Chattha, T. K. Geok, and B. A. Khawaja, "Compact wideband four-port MIMO Antenna for sub-6 GHz and internet of things applications," *Micromachines*, Vol. 13, No. 12, 2202, 2022.

[17] Floch, J. M. and I. B. Trad, "Design of multiband and wideband antennas with printed dipole," in *2015 IEEE 15th Mediterranean Microwave Symposium (MMS)*, 1–4, Lecce, Italy, 2015.

[18] Jean-Marie Floc, H. and A. E. S. Ahmad, "Dual-band printed dipole antenna with parasitic element for compensation of frequency space attenuation," *International Journal of Electromagnetics and Applications*, Vol. 2, No. 5, 120–128, 2012.

[19] Liao, W.-J., Y.-C. Lu, and H.-T. Chou, "A multiband microstrip dipole antenna," in *2005 IEEE Antennas and Propagation Society International Symposium*, Vol. 1A, 462–465, Washington, DC, USA, 2005.

[20] Patel, D. H. and G. D. Makwana, "Multiband antenna for 2G/3G/4G and sub-6 GHz 5G applications using characteristic mode analysis," *Progress In Electromagnetics Research M*, Vol. 115, 107–117, 2023.

[21] Khattak, M. K., C. Lee, H. Park, and S. Kahng, "A fully-printed CRLH dual-band dipole antenna fed by a compact CRLH dual-band balun," *Sensors*, Vol. 20, No. 17, 4991, 2020.

[22] Abdelkarim, M., A. Gharsallah, and R. Faouel, "Analysis and design of a high gain multiband antenna based on metamaterials for RFID applications," *International Journal of RF and Microwave Computer-Aided Engineering*, Vol. 2024, No. 1, 8948916, 2024.

[23] Dong, M., D. Shen, C. Ma, Z.-H. Ma, X. Li, and J. Su, "A novel split ring slot antenna with multiband characteristics based on SIW," in *2016 11th International Symposium on Antennas, Propagation and EM Theory (ISAPE)*, 39–42, Guilin, China, 2016.

[24] Vallappil, A. K., M. K. A. Rahim, B. A. Khawaja, and M. N. Iqbal, "A miniaturized metamaterial-loaded switched-beam antenna array system with enhanced bandwidth for 5G applications," *IEEE Access*, Vol. 12, 6684–6697, 2024.

[25] Chu, C., Y. Li, J. Wang, Y. Guo, and W. Wu, "A rectangular patch antenna with wideband harmonic suppression," *IEEE Antennas and Wireless Propagation Letters*, Vol. 22, No. 12, 3102–3106, 2023.

[26] Albishti, A. B., S. A. Hamzah, S. M. Shah, K. N. Ramli, N. Abdullah, M. S. Zainal, L. Audah, A. Ubin, F. C. Seman, A. K. Anuar, *et al.*, "Harmonic suppression dual-band dipole antenna with parasitic elements and a stub," *TELKOMNIKA (Telecommunication Computing Electronics and Control)*, Vol. 16, No. 5, 1918–1922, 2018.

[27] Hamzah, S. A., M. Esa, and N. N. N. A. Malik, "Reduced size harmonic suppressed fractal dipole antenna with integrated reconfigurability," in *2010 IEEE Asia-Pacific Conference on Applied Electromagnetics (APACE)*, 1–4, Port Dickson, Malaysia,

2010.

[28] Abd Azis, A. D., S. A. Hamzah, M. N. Dalimin, K. N. Ramli, M. S. Yahya, F. C. Seman, W. M. Utomo, B. A. Khawaja, S. Nordin, *et al.*, "Dual band LoRa/GPS dipole antenna with harmonic suppression capability," in *2025 2nd International Conference on Advanced Innovations in Smart Cities (ICAISC)*, 1–3, Jeddah, Saudi Arabia, 2025.

[29] Hamzah, S. A., F. C. Seman, S. M. Shah, K. N. Ramli, M. S. Zainal, M. M. Som, M. S. Mustapa, M. Esa, N. N. N. A. Malik, L. Audah, and N. Abdullah, "A triple-band dipole antenna with harmonic suppression capability," *International Journal of Integrated Engineering*, Vol. 12, No. 3, 131–137, 2020.

[30] Zhou, Y., T. Jiang, H. Li, and F. Chen, "A 5G MIMO multiband low-profile antenna design for automotive shark-fin systems," *IEEE Antennas and Wireless Propagation Letters*, Vol. 23, No. 5, 1588–1592, 2024.

[31] Tawk, Y., K. Y. Kabalan, A. El-Hajj, C. G. Christodoulou, and J. Costantine, "A simple multiband printed bowtie antenna," *IEEE Antennas and Wireless Propagation Letters*, Vol. 7, 557–560, 2008.

[32] Nejdi, I. H., Y. Rhazi, M. A. Lafkih, and S. Bri, "Designing multiband multilayered microstrip antenna for UMTS, ISM, communication satellite, HiperLAN and C-band," in *2018 International Symposium on Advanced Electrical and Communication Technologies (ISAECT)*, 1–8, Rabat, Morocco, 2018.

[33] Boukarkar, A., X. Q. Lin, Y. Jiang, and Y. Q. Yu, "Miniaturized single-feed multiband patch antennas," *IEEE Transactions on Antennas and Propagation*, Vol. 65, No. 2, 850–854, 2017.

[34] Su, S.-W. and Y.-L. Kuo, "Multiband, dual-strip biplanar monopole for internet of things applications," in *2024 International Symposium on Antennas and Propagation (ISAP)*, 1–2, Incheon, Korea, 2024.

[35] Huang, H., Y. Liu, S. Zhang, and S. Gong, "Multiband metamaterial-loaded monopole antenna for WLAN/WiMAX applications," *IEEE Antennas and Wireless Propagation Letters*, Vol. 14, 662–665, 2014.